Electrocatalytic transformation of HF impurity to H_2 and LiF in lithium ion batteries

Dusan Strmcnik[1*], Ivano E. Castelli[2], Justin G. Connell[1], Dominik Haering[3], Milena Zorko[1], Pedro Martins[1], Pietro P. Lopes[1], Bostjan Genorio[1], Thomas Østergaard[2], Hubert Gasteiger[3], Filippo Maglia[4], Byron K. Antonopoulos[4], Vojislav R. Stamenkovic[1], Jan Rossmeisl[2*] and Nenad M. Markovic[1]

[1]Materials Science Division, Argonne National Laboratory, Argonne, IL 60439

[2]Nano-Science Center, Department of Chemistry, University of Copenhagen, DK-2100 Copenhagen, Denmark

[3]Chair of Technical Electrochemistry, Department of Chemistry and Catalysis Research Center, Technische Universität, München, D-85748 Garching, Germany

[4]BMW Group, Battery Cell Technology, 80788 München, Germany

The formation of solid electrolyte interphase (SEI) on graphite anodes plays a key role in the efficiency of Li-ion batteries. However, to date, fundamental understanding of the formation of LiF as one of the main SEI components in hexafluorophosphate-based electrolytes remains elusive. Here, we present experimental and theoretical evidence that LiF formation is an electrocatalytic process that is controlled by the electrochemical transformation of HF impurity to LiF and H_2. Although the kinetics of HF dissociation and the concomitant LiF/H_2 production is dependent on the structure and nature of surface atoms, the underlying electrochemistry is the same. The morphology, and thus the role, of the LiF formed is strongly dependent on the nature of the substrate and HF inventory, leading to either complete or partial passivation of the interface. Our finding is of general importance and may open new opportunities for the improvement of existing, and the design of new, Li-ion technologies.

Advancing and deploying renewable energy technologies requires the application of experimental and computational methods capable of characterizing solid-aqueous and solid-organic electrochemical interfaces at atomic and molecular levels. Whereas fundamental understanding of the forces that control the efficiency of solid-aqueous interfaces is rather advanced[1–5], the picture of solid-organic interfaces is still quite hazy due to the lack of complementary information about structure-function relationships in organic solvents. For example, despite decades of research into Li-ion batteries (LIB), whose performance largely depends on the formation of the so-called "solid electrolyte interphase" (SEI) on the graphite anode, detailed mechanistic understanding of the nature of SEI

formation and its resulting structure remains elusive[6–11]. As a result, the development of electrolytes for LIB remains a somewhat empirical process, with the most common electrolytes consisting of a combination of lithium hexafluorophosphate ($LiPF_6$) salt with a binary solvent mixture of cyclic and linear alkyl carbonates such as ethylene carbonate (EC) and ethyl methyl carbonate (EMC). The selection of these electrolytes is based on their high salt solubility, high ionic conductivity and on the formation of a stable SEI that simultaneously minimizes electrolyte decomposition while still providing high Li^+ diffusivity[12].

The morphological and compositional picture of the SEI formed in such environments is complex, involving numerous proposed reaction products; with solid $LiF_{(s)}$ consistently found as one of the main SEI components[8,13–15]. It is generally accepted that the formation of $LiF_{(s)}$ can occur through both chemical reactions of $LiPF_6$ with water or HF with organic/inorganic carbonates, as well as through the electrochemical reduction of PF_3O and/or PF_6^- [16–19]. Although plausible, it has never been confirmed experimentally that these reactions do indeed lead to the formation of $LiF_{(s)}$. One report, however, provided some evidence that the formation of $LiF_{(s)}$ could also be controlled by the electroreduction of HF[20], the latter being a highly detrimental product that is formed in the reaction between trace levels of H_2O and $LiPF_6$ [21–27]. Impurity levels of HF present in organic electrolytes can affect all components of the battery, impacting the formation of the SEI as well as inducing dissolution (corrosion) of the oxide cathode materials and inactive components of the cell[28–31]. All of these processes can significantly affect battery performance, and as a result understanding the role of HF electrochemistry in EC/EMC/$LiPF_6$ electrolytes at atomic and molecular levels would contribute immensely to current understanding of the fundamental electrochemistry of Li-ion battery electrolytes.

The study reported herein identifies the electrocatalytic transformation of HF to $LiF_{(s)}$ and H_2 in EC/EMC/$LiPF_6$ electrolytes by utilizing a surface science-based strategy that has been successfully used in the past to unravel the complexities controlling the efficiency of energy conversion and storage processes at solid-aqueous electrochemical interfaces[32–35]. The formation of $LiF_{(s)}$ and H_2 is first explored on well-characterized single crystals of Ir(111), Pt(111), Au(111) and Cu(111) and graphene-modified Pt(111). Then, the knowledge gained from model systems is translated to carbon-based materials; ranging from basal plane and edge-exposed highly ordered pyrolytic graphite (HOPG) to real graphite anodes. From experimental and computational trends established on single crystals, we found that HF dissociation and concomitant $LiF_{(s)}$ and H_2

formation are governed by a synergy between the nature of surface atoms and potential-driven covalent and non-covalent interactions in the double layer. Beyond mechanistic understanding, these results provide insights into the previously overlooked importance of electrocatalysis in the formation of $LiF_{(s)}$ and H_2 on metals, graphene, basal plane/edge-exposed HOPG, and more realistic graphite powder surfaces in organic electrolytes. Furthermore, our approach reveals intriguing relationships between the substrate-controlled morphology of and passivation by $LiF_{(s)}$, as well as between the density of surface defects and the kinetics of electrolyte decomposition. Taken together, the results reveal that $LiF_{(s)}$ precipitation and H_2 evolution during SEI formation in LIBs is, in fact, controlled by an interplay between the electrochemical and chemical reactivity of two impurities - H_2O and HF.

Results

Electrochemistry of H_2O and HF on metal single crystals. We begin by evaluating the concentration of various organic and inorganic impurities that are present in commercially-available 1M $LiPF_6$ in EC:EMC (3:7 wt%) electrolytes (commercially known as LP57 and hereafter referred to simply as 1M $LiPF_6$), with particular interest in determining the concentration of the two most significant impurities – H_2O and HF[21,25–27]. While the amount of water in the electrolytes was determined using a standard Karl-Fischer titration, a novel method was implemented for the determination of HF. A 100 µL of sample electrolyte was injected into 10 mL of total ion strength adjustment buffer (TISAB) and the concentration of fluoride ion was determined with fluoride ion-selective electrode (ISE) using a calibration curve generated with previously prepared standards. Perhaps counterintuitively, the dilution of the non-aqueous sample of $LiPF_6$ in TISAB essentially quenches any further hydrolysis of $LiPF_6$, which makes such analysis possible. (For more details see Supplementary Methods, Supplementary Figure 1 and Supplementary Table 1). The concentration of HF and H_2O in as-received, commercial 1M $LiPF_6$ was found to be in the range of 30-60 ppm and 1-5 ppm, respectively, with the markedly lower H_2O concentration resulting from the slow, but quantitative, conversion of H_2O to HF. In order to measure the rate of this conversion, a fixed quantity of water was added to homemade 1M $LiPF_6$ and the concentrations of H_2O and F^- were measured as a function of time. As shown in Figure 1, for the initial value of HF present in the as-prepared electrolytes (~20ppm), the addition of 50, 100

and 150 ppm of water resulted in the formation of 120, 220 and 300 ppm of HF, as expected based on the reactions:

$$LiPF_6 \leftrightarrow LiF + PF_5 \quad (1)$$

$$H_2O + PF_5 \rightarrow 2HF + POF_3 \quad (2)$$

One mole of H_2O leads to the formation of two moles of HF (for details see methods section). The ability to control and quantitatively measure the transformation of H_2O into HF in 1M $LiPF_6$ served as an important method to explore how different concentrations of HF may affect the electrochemistry, as discussed below.

In order to demonstrate a strong link between the chemistry of HF in $LiPF_6$ electrolytes and the electrocatalytic dissociation of water in aqueous electrolytes, we will first summarize trends in the hydrogen evolution reaction (HER) on Cu(111), Au(111), Ir(111) and Pt(111) in 0.1 M KOH (Figure 2a). The HER in alkaline solutions is usually assumed to proceed by the following reaction steps[36]:

$$H_2O + e^- \rightarrow H_{ad} + OH^- \quad (3)$$

$$2H_{ad} \rightarrow H_2 \quad (4)$$

where H_{ad} is the adsorbed reactive intermediate. The rate of this reaction is strongly dependent on the nature of the electrode material and increases in the order Cu(111) < Au(111) << Pt(111) < Ir(111), a fact that arises due to differences in the water dissociation step (Cu > Ir > Pt > Au)[37,38] and the metal-H_{ad} binding energy (Ir ~ Pt >> Au ~ Cu)[39,40]. An optimal balance between these two descriptors results in activity that decreases in the order Ir(111) > Pt(111) >> Au(111) > Cu(111). The same trend is observed for polarization curves recorded on these single crystal surfaces in 1M $LiPF_6$ (Figure 2b), suggesting that the reaction steps in this organic electrolyte may be conceptually similar to those involved in H_2 production from H_2O[41]. A noticeable difference is that for all surfaces depicted in Figure 2b, an initial exponential increase in current is followed by a rather fast deactivation and very little activity during subsequent sweeps (for Au(111) see Supplementary Figure 2), indicating passivation from surface product(s) that are formed in the course of the reaction (in line with Li-O_2 electrochemistry in organic environments[42]).

The morphology and chemical nature of the deposit were explored by combing *ex situ* atomic force microscopy (AFM) and X-ray photoelectron spectroscopy (XPS). For clarity we summarize only results for Au(111) as a representative of single crystals considered in this work (Figures 2c and 2d). A close inspection of AFM images reveals the presence of a compact, crack free, film with large (ca. 50-100 nm) 2D grain size domains (Figure 2c), while the chemical analysis of this film via XPS (Figure 2d) indicated that it consists predominately of $LiF_{(s)}$ and a small amount of either $LiP_xO_yF_{z(s)}$ formed from side reactions or, even more likely, $LiPF_6$ due to residual salt not removed during sample rinsing (for more details see Supplementary Figures 7-9 and Supplementary Table 2). We note that the SEI peak positions are shifted to slightly higher binding energy (BE) than expected due to differential charging of the highly insulating LiF layer relative to the conductive substrate [43]. This phenomenon is quite common when analyzing SEI layers on Li-ion battery electrodes but is seldom discussed, leading to a large spread in BE values for SEI components reported in the literature[8]. Based on these results and a complementary experiment, where the composition of the dissolved film was probed by inductively coupled plasma mass spectrometry (ICP-MS) and fluoride ion selective electrode (ISE) measurements (for details see Supplementary Table 1), we concluded that a compact layer of $LiF_{(s)}$ is formed on Au(111), as well as other single crystal metal surfaces, during the first cathodic sweep. In order to develop mechanistic insights into the process(es) that may lead to $LiF_{(s)}$ formation, we made use of the rotating disk electrode (RDE) method to explore how the current-voltage traces shown in Figure 2b are affected by both the rotation rate of the electrode and the concentration of HF (Figure 2f). As displayed in Supplementary Figure 3 for Au(111), the current increases with increasing rotation rate for the same concentration of HF, indicating that the reaction is mediated by the transport of at least one of the reactants to the electrode surface and that the reactant is present in small concentration (i.e. its supply is limited). Notice also that although diffusion-limited currents are never established because of potential-dependent surface passivation by $LiF_{(s)}$ (i.e. currents don't follow a Levich-type behavior), the peak current and the corresponding charge still increases with rotation rate. Furthermore, systematic variation of the concentration of HF in 1M $LiPF_6$ between 30 and 300 ppm (Figure 2f) yields a linear increase of the kinetic current density with increasing HF concentration, strongly suggesting that the reduction process is controlled by HF electrochemistry. Additional confirmation is provided by the fact that no reaction takes place between 2.0-2.5 V in 1M $LiClO_4$ (Figure 2e).

Based on the above experimental evidence, it is plausible to conclude that the reduction process(es) observed during the very first potential sweep from 3.5 V to 1.5 V is governed by the surface electrochemistry of HF reduction; e.g., the dissociation of HF and subsequent H_2 production according to reactions (5) and (6):

$$HF + e^- \rightarrow H_{ad} + F^- \quad (5)$$

$$2H_{ad} \rightarrow H_2 \quad (6)$$

$$F^- + Li^+ \rightarrow LiF_{(s)} \quad (7)$$

A schematic representation of the proposed processes that control H_2 and HF production is given in Figure 3, and is also supported by Density Functional Theory (DFT) calculations that are described in detail in the Supplementary Methods. As summarized by reactions 5-7, the potential-controlled dissociative adsorption of HF leads to the formation of H_{ad} and F^- which, in an electrochemical-chemical reaction scheme, are very quickly transformed to H_2 and $LiF_{(s)}$. In line with the HER in aqueous environments, it is likely that the kinetics of the HER in 1M $LiPF_6$ are directed by an optimal balance between the energy required for the dissociation of HF and the metal-H_{ad} binding energy; supporting the proposition that there are inherently close ties between interfacial phenomena in aqueous and organic environments – a very important subject that has rarely been discussed[2].

Besides the obvious similarities between aqueous and organic environments there are also important differences between the HER in alkaline and EC/EMC/$LiPF_6$ electrolytes. By comparing Figure 2a and 2b it is obvious that, in contrast to OH^- in alkaline solution, the generated F^- ions in reaction (7) readily react with Li^+ ions present in the double layer of the metal-1M $LiPF_6$ interface. This in turn, results in the formation of spectator $LiF_{(s)}$ that blocks the metal active centers required for the HER to take place. In addition to this surface poisoning effect, deactivation of the HER is also caused by the diffusion-limited transport of HF to the electrode surface. Taken together, the shape of the current-voltage curves in Figure 2b is controlled by a delicate balance between the transport of the HF to the surface, the kinetics of electrochemical reduction of HF to H_2 on metal surfaces (Eq. 5 and 6) and the kinetics of $LiF_{(s)}$ formation in the double layer and its passivation of the metal surfaces (eq. 7). We note that our mechanistic insight differs significantly from a previous hypothesis that the first reduction peak centered at ca. 2.5V is the result of the so-called underpotential deposition of hydrogen (H_{upd})[20] during HF reduction on polycrystalline Pt. In particular, our results

for Cu(111) and Au(111), which do not form H_{upd} but show the same behavior as Pt(111) and Ir(111) (Figure 2b), clearly demonstrate that the sharp peak is caused by the HER rather than the formation of H_{upd}. Note also that purely kinetic current for the HER from HF is observed only in the early stages of the electroreduction process between 2.5-2.25 V. In this potential range, the current is linearly dependent on the concentration of HF. The total charge under individual curves, however, approaches a constant value with increasing HF concentration (Supplementary Figure 4), consistent with precipitation of $LiF_{(s)}$ at or near the electrode that lags behind the electrochemical HER step but ultimately leads to passivation of the active surface. As we discuss further below, the kinetics of these processes, as well as the thickness and morphology of $LiF_{(s)}$, are critically dependent on the nature of the substrate.

Electrochemistry of HF on carbon systems. In order to bridge the gap between the model systems discussed above and real graphitic anode materials, HF electrochemistry in 1M $LiPF_6$ was examined on multilayer-graphene (MLG) synthesized on Pt(111) single crystals via chemical vapor deposition (CVD, for details see methods section). The Pt(111)-MLG offers the closest possible approximation to a defect-free, well-ordered graphite surface, as shown by a combination of Crystal Truncation Rod (CTR) and Scanning Tunneling Microscopy (STM) measurements that indicate the presence of ca. 5 layers of graphene on Pt(111) (Supplementary Figures 10 and 11) and that the topmost layer of graphene is nearly defect-free (Supplementary Figure 10). A representative electrochemical response on such a surface (Figure 4a) reveals that the main voltammetric feature on the negative sweep direction from 3.25 V is a sharp peak at ~0.25 V, which is ~2 V more negative than that observed on the rather inactive Au(111) surface. This sharp peak, which is enlarged by increasing both the rotation rate and the concentration of HF (Figure 4b), is associated with the HF-controlled production of H_2 and $LiF_{(s)}$ by analogy with related processes on single crystals (see eqs. 5-7). Under our experimental conditions, the XPS analysis (Supplementary Figures 8-9) confirms that the main surface product formed below 1.0 V is $LiF_{(s)}$. The difference in reactivity between metal surfaces and graphene is in good agreement with the intrinsically high energy barrier required for splitting HF (attenuating the dissociation kinetics), accompanied by lower availability of non-specifically adsorbed Li^+ (due to the lower work function, Supplementary Figure 16) and a weak graphene-H_{ad} interaction (reducing the surface coverage by H_{ad}). Note that no organic or inorganic carbonates were found in the SEI on MLG

(Figure 4d), indicating unique properties of this carbon surface as compared to other carbon samples found in the literature.

In contrast to single crystal surfaces (Figure 2), subsequent cycles on Pt(111)-MLG (Supplementary Figure 5) do not exhibit the strong deactivation due to surface passivation, indicating that the film morphology may vary between metal and graphitic substrates. Indeed, AFM images of $LiF_{(s)}$ on graphene (Figure 4c) reveal a highly porous, granular film (grain size 10-30 nm), with a RMS roughness 5 times higher relative to films formed on single crystal metals (Figure 2c and Supplementary Table 3). Cracks and grain boundaries in the film are also observed on both small and larger scales (20x20 μm, Supplementary Figure 12), in contrast with films formed on metal surfaces. As such, it is plausible to expect the film to be permeable to species from the electrolyte, which may explain, at least qualitatively, why $LiF_{(s)}$ does not passivate graphene surfaces for further HF reaction in subsequent cycles.

Additional insight into the morphological role of the substrate on the SEI layer can be gleaned by comparing HF electrochemistry on more defected HOPG surfaces, which are even closer in structure to real graphite anode materials. Electrochemical results are summarized in Figures 4e and 4f for basal plane and edge-exposed HOPG, respectively. In agreement with previous findings[44], the very first polarization curve recorded on basal plane shows two sharp reduction peaks at 0.7 and 0.25 V. During the second potential excursion, the more positive peak completely vanishes, whereas the peak at 0.25 V remains unchanged even after several consecutive cycles, resembling the behavior of this feature observed for graphene. In agreement with graphene electrochemistry, the current density for the reduction process at 0.25 V is enhanced as the rotation rate (Supplementary Figure 6) and concentration of HF are increased, suggesting that this process is also controlled by HF dissociation and $LiF_{(s)}/H_2$ formation. On the other hand, the reduction peak at 0.7 V was only observed in the first scan and was highly dependent on the cleavage of the HOPG substrate, which indicates that the density of defects such as step edges and other defects on HOPG may control the kinetics of this process. XPS analysis of the C1s of HOPG surfaces reveals the presence of C=O (287.0 eV), R-OCO_2Li (~291 eV) and CO_3 (~291 eV) species[8,18,44] that are not observed on Pt(111)-MLG surfaces (Figure 4d). At this point, we do not have any direct evidence to explain the absence of solvent decomposition/carbonate formation on graphene, however, the appearance of the additional feature at 0.7V on HOPG surfaces along with

the additional features in the C 1s strongly indicate that this electrochemical feature is related to solvent decomposition on HOPG. The role of defects was further probed on edge-exposed HOPG (Figure 4f), where a tremendous increase in the reduction current below 0.8 V was observed, completely obscuring the formation of $LiF_{(s)}$ and H_2 by simultaneous electrolyte decomposition and/or Li intercalation processes[45–49]. In our opinion these observations, along with the strong dependence of the electrochemical response on the HOPG cleavage, warrants the explanation that surface defects on graphite, which are to a large extent absent on our graphene sample, are most likely the active sites for solvent decomposition. Note also that almost no LiF was found on HOPG surfaces when the potential window was closed to 0.5 V vs. Li/Li^+. As shown in Supplementary Figure 7, significant LiF formation on HOPG or graphene does not take place until electrodes are cycled through the electrochemical process at 0.25 V. This directly opposes the proposed mechanism of LiF formation that is often found in the literature, which suggests that surface carbonates react with HF and produce $LiF_{(s)}$ [16,17,23,29].

Electrochemistry of HF in real systems. To close the loop, we directly monitored H_2 production on real, high surface area graphitic anode materials in order to understand the influence of HF content on the HER in 1M $LiPF_6$ under battery operating conditions. Both RDE and On-line Electrochemical Mass Spectrometry (OEMS) were used to explore HF electrochemistry on SLP30 graphite in 1M $LiPF_6$ electrolytes containing 60 or 260 ppm HF. Figure 5a shows the first reductive voltammetric scan obtained either on a SLP30 graphite-coated RDE (0.3 mg_{SLP30} cm^{-2}_{disk} at 50 mV s^{-1}) or in a SLP30//LFP cell (4.7 mg_{SLP30} cm^{-2}_{disk} at 0.2 mV s^{-1}) connected to the OEMS. In the first potential cycle from 3.5 V the first current onset in RDE curves recorded at 50 mV s^{-1} (Figure 5a) was observed at ~2 V, followed by a sharp increase in activity at ca. 0.5 V. Not surprisingly, due to the very slow sweep rate for polarization curves recorded in the OEMS setup (0.2 mV s^{-1}), it was very difficult to obtain clear cut evidence at what potential the first reaction might start. As in the past, however, OEMS provides quantitative information about the potential-dependent production of gases that can be formed in the course of the reaction, as summarized in electrolytes containing 60 ppm (Figure 5b) and 260 ppm (Figure 5c) of HF. Several observations are noteworthy. First, a four-fold increase in HF concentration produces roughly a four-fold increase in hydrogen production (indicated by the accumulated amount of H_2 in the OEMS cell at the end

of the reductive voltammetric scan, i.e., at 0 V), which confirms the correlation between HF concentration and the amount of evolved hydrogen. Second, the HER onset is observed at ~2 V, suggesting that the currents observed in the RDE experiment are most likely due to H_2 production. Third, it is plausible that the small, yet clearly discernable, currents starting at ~2V on model carbon systems under the same experimental conditions (Figures 4, S5, and S6) can also be linked to HF reduction to H_2. That H_2 formation is clearly observable in OEMS experiments is due to the 20 times higher active surface area of SLP30 graphite than graphene or HOPG samples, which leads to a significant increase in the number of active surface sites, possibly surface defects, and thus higher currents. Finally, the evolution of C_2H_4 (a well-known product of the reduction of ethylene carbonate) and CO (a minor reduction product) initiates just below 1.0 V vs. Li/Li^+, which is identical to the previously reported onset potential and C_2H_4/CO ratio[50] and clearly indicates that the LiF formed from the reduction of HF does not result in a sufficiently passivating surface to prevent ethylene carbonate reduction.

As expected, there are differences and similarities between model experiments in an RDE configuration and real battery cells. Although the chemistry does not really change from the model to real system, the relative abundance of SEI components as well as the onset of their production does. We argue that this is mainly caused by the significantly larger ratio of electrode surface area to electrolyte volume (~10^6 times) for the graphite electrode in the OEMS cell compared to well-defined surfaces in the three-electrode electrochemical cell. This difference likely introduces a significant amount of surface defects, as well as imposes a restriction on the maximum possible LiF surface coverage[31] on graphite that can be achieved upon complete reduction of all residual HF in in the OEMS cell. In a typical battery cell this will result in the formation of only one or two monolayers of LiF, compared to several nanometers in a typical RDE configuration.

Nevertheless, the above experimental results indicate that simultaneous formation of $LiF_{(s)}$ and H_2 in 1M $LiPF_6$ on anode electrodes is much simpler than considered thus far. Through systematic investigation it was possible to gain fundamental understanding of how the synergy between the structure and nature of surface atoms, covalent and non-covalent forces, and ppm-levels of electrolyte (H_2O and HF) as well as electrode material defects control the electrocatalytic dissociation of HF and the concomitant adsorption of H_{ad} (HER), the interaction of F^- and Li^+ and the precipitation of LiF, a key part of the SEI. Although this work does not directly address the

role of LiF in battery performance, it creates a platform for such understanding. We conclude that our finding is of general importance and we believe it will open new opportunities for the improvement of existing systems and the design of new LIB technologies.

Methods

Extended surface electrode preparation: Pt(111), Ir(111), Au(111), Pt-poly and Ir-poly electrodes were prepared by inductive heating for 5 min at 1,050 °C for Pt, 800 °C for Au and Cu and 1,200 °C for Ir electrodes in an argon hydrogen flow (3% hydrogen). The annealed specimens were cooled slowly to room temperature under an inert atmosphere and then assembled into a rotating disk electrode (RDE). Voltammograms were recorded in argon-saturated electrolytes.

Preparation of carbon samples: Multi-layer graphene was grown on Pt(111) heated to 1,050 °C in methane flow. The HOPG ZYA type crystal with basal exposed plane (Princeton Scientific Corp) was assembled into RDE and freshly cleaved with adhesive tape inside the glove box prior to each experiment. The HOPG ZYA type crystal with edge exposed plane (Princeton Scientific Corp) was cut parallel to the edge surface with a stainless-steel blade to expose fresh surface and subsequently washed with EMC, dried and inserted into RDE. SLP30 graphite powder (TIMREX by Imerys Graphite & Carbon, Switzerland, BET surface area ~7 m^2/g) was dry-casted from an EMC suspension onto a glassy carbon electrode assembled into RDE with a loading of 0.3 mg/cm^2. For OEMS experiments SLP30 graphite was prepared as an ink with PVDF and NMP and then blade-coated onto a porous Celgard separator (for more details see SI). In both cases the electrode with SLP30 was dried overnight in a vacuum oven at 95 °C.

Chemicals: For aqueous experiments 0.1 M KOH was prepared from highest purity Sigma Aldrich KOH and Millipore Milli-Q water. For non-aqueous experiments LP57 (1M $LiPF_6$ in EC:EMC (3:7 wt)) purchased from BASF, or homemade 1M $LiPF_6$ prepared from EC, EMC and $LiPF_6$ (all from BASF) were used. Argon gas used for purging was 5N5 quality and purchased from Airgas. 1M $LiPF_6$ electrolytes with various concentrations of HF were prepared by adding the appropriate amounts of water to homemade 1M $LiPF_6$ and waiting for 2 weeks for the H_2O concentration to fall below 5 ppm (see also main text and SI). Note that according to reactions (1) and (2), LiF is also formed in this process. However, this LiF stays as a precipitate in the electrolyte container and does not make it into the electrochemical cell.

Water and HF determination: Water content in electrolytes was measured using Karl Fischer titration (Metler-Toledo) placed inside an Ar filled glovebox with H_2O level below 0.5 ppm. HF content was measured using fluoride ISE (Mettler Toledo perfectION combination fluoride electrode) in our newly-developed method for fluoride determination in $LiPF_6$ electrolytes. Low level TISAB of the following composition was used for all fluoride measurements: 57 mL glacial acetic acid, 58 g sodium chloride dissolved in water in 1L volumetric flask and with pH adjusted to 5.0-5.5 with 1M NaOH (all chemicals were purchased from Sigma-Aldrich).

Electrochemical measurements: With the exception of OEMS experiments (See Supplementary Methods), a three-electrode glass cell was used in all experiments. All of the experiments executed in this cell were performed within minutes of introducing the electrolyte into the cell, thus preventing significant reaction of HF with the glass. Furthermore, fluoride ISE measurements before and after electrochemistry reveal no significant changes in the HF concentration, further indicating that there is no significant reaction of HF with the glass. Finally, XPS measurements of electrode surfaces reveal no evidence of Si, indicating that there is no participation of dissolved SiO_x in the reactions studied. Gold wire was used as a counter electrode and Ag/AgCl or Ag/Ag^+ electrode was used as reference electrodes for aqueous and non-aqueous experiments, respectively. All potentials are given either on a RHE scale or Li/Li^+ scale. The conversion of Ag/Ag^+ to Li/Li^+ scale was done by electrodepositing and stripping Li on a glassy carbon electrode in a separate experiment, establishing the position of the Li/Li^+ reversible potential. Experiments were controlled using an Autolab PGSTAT 302N potentiostat. For the rotating disk experiments, a Pine MSR electrode rotator was used. All reported polarization curves and voltammograms were first cycle measurements (unless explicitly stated otherwise) to limit the effects of possible contamination from the electrolyte. All non-aqueous electrochemical experiments were performed inside the glovebox.

XPS Measurements: XPS measurements were performed using a Specs PHOIBOS 150 hemispherical energy analyzer using a monochromated Al Kα X-ray source. The load-lock of the analytical UHV system is connected directly to an Ar-filled glove box, enabling the loading of samples without any exposure to ambient atmosphere. Survey spectra were measured using a pass energy of 40 eV at a resolution of 0.2 eV/step and a total integration time of 0.2 sec/point. Core level spectra were measured using a pass energy of 20 eV at a resolution of 0.05 eV/step and a total integration time of 0.5 sec/point. A charge neutralizing electron flood gun was used for some samples to attempt to address differential charging between highly insulating LiF and conductive substrates. Deconvolution was performed using CasaXPS software with a Shirley-type background and 70-30 Gaussian-Lorentzian peak shapes. In general, spectra were charge referenced using the position of the Au $4f_{7/2}$ at 84.0 eV, Pt $4f_{7/2}$ at 71.2 eV and C 1s at 284.0 eV for Au, Pt-MLG and HOPG samples, respectively. See the Supplementary Methods for a detailed discussion of charge referencing, differential charging and charge compensation on these samples.

AFM Measurements: After electrochemical measurements, the samples were taken out of the glovebox and transferred to Bruker's Dimension Icon AFM in a vibration isolation enclosure for imaging. A Si TESPA-V2 tapping tip was used to obtain the images.

DFT Calculations: The calculations are done using the GPAW code[51,52] and the structures as well as the molecular dynamics is run by means of the ASE package.[53] The calculations are performed using RPBE as exchange-correlation functional[54], a single k-point (Gamma), and we apply the dipole correction to handle

in the correct way the electrostatic potential in the z-direction at the periodic boundary condition. The characteristic time for the Berendsen termostat was set to 2000 fs and the time step to 1 fs. This procedure has been previously applied by Hansen and Rossmeisl to water[55]. (For more details see Supplementary Methods)

Data availability: All data is available from the authors upon reasonable request

Figures:

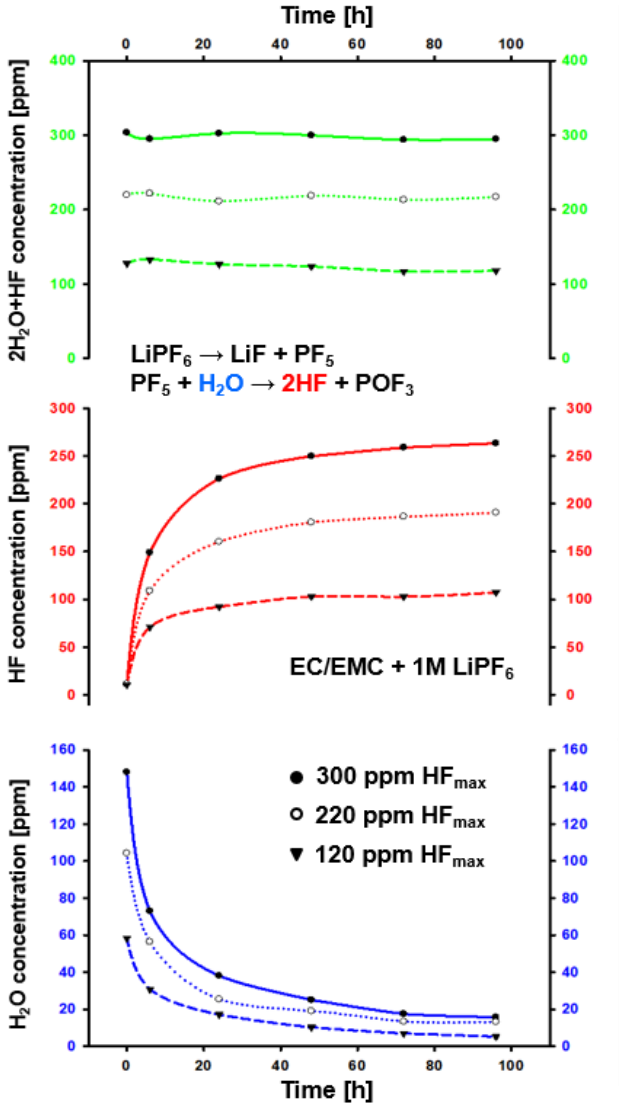

Figure 1: Chemical transformation of H_2O to HF in 1M $LiPF_6$. The concentrations of water (blue) and HF (red) as a function of time after the addition of different concentrations of water (50, 100, and 150 ppm) to 1 M $LiPF_6$ in EC:EMC (3:7 wt%). [HF] was measured with a fluoride ion-selective electrode and [H_2O] was measured via Karl-Fischer titration. The total H concentration (green), presented as the sum 2[H_2O] + [HF], is constant and confirms the quantitative transformation of H_2O to HF in a 2:1 ratio. Note that i) the starting values for HF are 20 ppm for the as prepared electrolyte which affect the final HF concentration after the addition of water and ii) the final values of HF are not reached after 96 hours. After 14 days, the water concentrations were 4.9, 2.5 and 2.1 ppm and the HF concentrations were close to the maximum values depicted in green, i.e. 300 ppm, 220 ppm and 120 ppm respectively. Finally, the HF ppm were

divided by 1.1 in order to compare stoichiometry, based on molar masses 20 and 18 g/mol for HF and H_2O, respectively

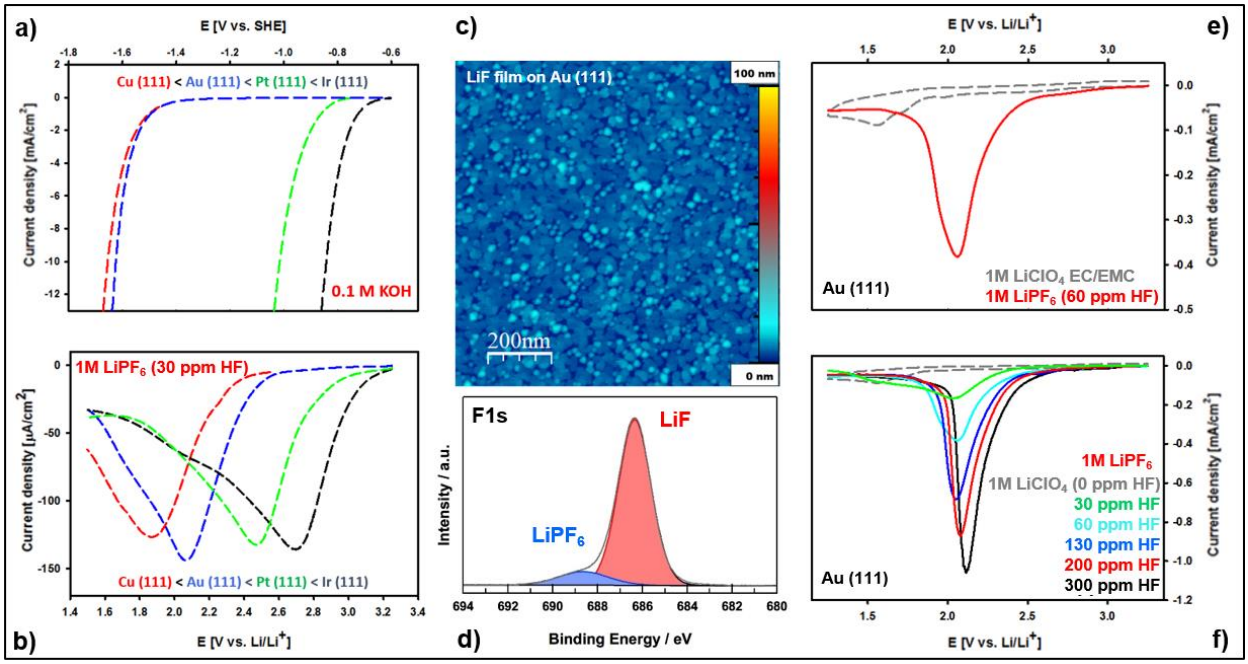

Figure 2: Electrocatalytic transformation of HF to LiF and H_2 on well-defined metal surfaces. a) HER trend on 4 metal single crystal surfaces in 0.1 M KOH. b) HER trend on same surfaces in 1M $LiPF_6$. c) AFM image of LiF film on Au (111) surface after 2 potential sweeps from 3.3 to 1.25 V vs. Li/Li^+. d) F 1s XPS spectrum of Au(111) after two potential sweeps from 3.3 to 1.25 V vs Li/Li^+. The formation of $LiF_{(s)}$ was further confirmed by utilizing a combination of (ICPMS) and fluoride (ISE) to quantify the ratio between Li^+ and F^- produced after dissolution of the "SEI film" in water (see also the Supplementary Methods and Supplementary Table 1). Li and F were found to be in a 1:1 stoichiometric ratio, with the amount corresponding to a ~2.5 nm thick film (if compact). e) Electrochemical response of Au (111) in 1M $LiPF_6$ containing 60 ppm of HF and in HF-free EC:EMC (3:7 wt%) with 1M $LiClO_4$. f) Dependence of the main electroreduction peak on Au (111) on the concentration of HF – different concentrations of HF were obtained by adding the appropriate amounts of water to home-made 1M $LiPF_6$. The measurement in 1M $LiClO_4$ is taken as 0 ppm HF. HF concentration was measured prior to and after the electrochemical experiment. All curves were measured with a sweep rate of 50 mV/s.

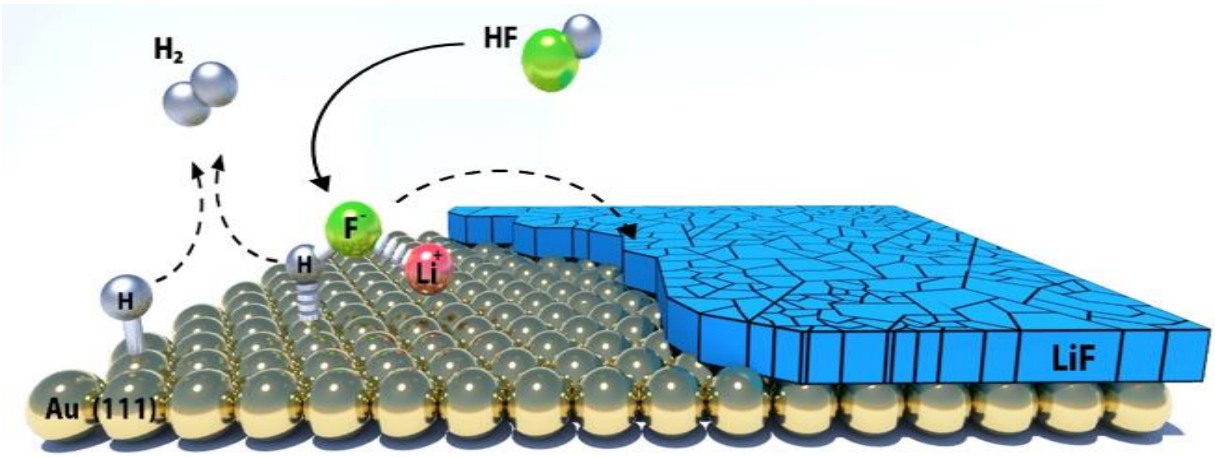

Figure 3: Schematic of the proposed reaction mechanism for the electrocatalytic conversion of HF into H_2 and LiF. The thickness of the LiF film, as well as its morphology, is affected by the kinetics of the electrochemical reaction (5), transport of the reactant HF, and the kinetics of the LiF crystallization process (7). Density Functional Theory (DFT) calculations have pointed out that there is a correlation between the first electrochemical response and the non-specific adsorption potential of Li^+ for the different investigated metals (Supplementary Figure 15b). This also suggests that the non-specific adsorption of Li^+ plays a critical role in the splitting of HF, as shown in the schematics and in the reaction path in Supplementary Figure 15a. It seems, in fact, that the presence of Li^+ in the double layer reduces the barrier for the dissociation of the HF molecule (more details are available in the Supplementary Methods).

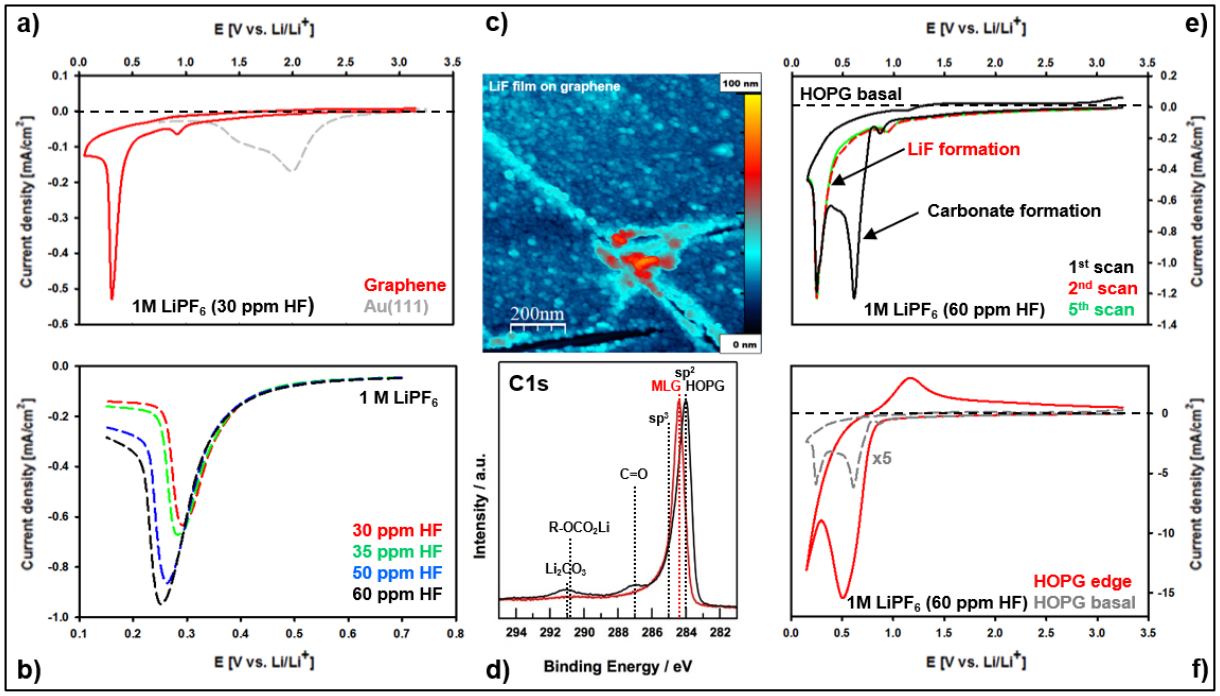

Figure 4: Electrocatalytic transformation of HF to LiF and H_2 on well-defined carbon surfaces. a) Electrochemical response of Pt(111)-MLG in 1M $LiPF_6$ compared to Au(111) in the same electrolyte. b) Dependence of the main cathodic peak on the concentration of HF. c) AFM image of the LiF film on graphene after 1 potential scan from 3.5 V – 0.1 V vs. Li/Li^+ d) XPS C 1s spectra of Pt(111)-MLG and basal plane HOPG after a potential excursion to 0.25 V vs. Li/Li^+, respectively. e) Electrochemical response of basal plane HOPG in 1M $LiPF_6$. f) Electrochemical response of edge-exposed HOPG in 1M $LiPF_6$. All measurements were performed at 50 mV/s.

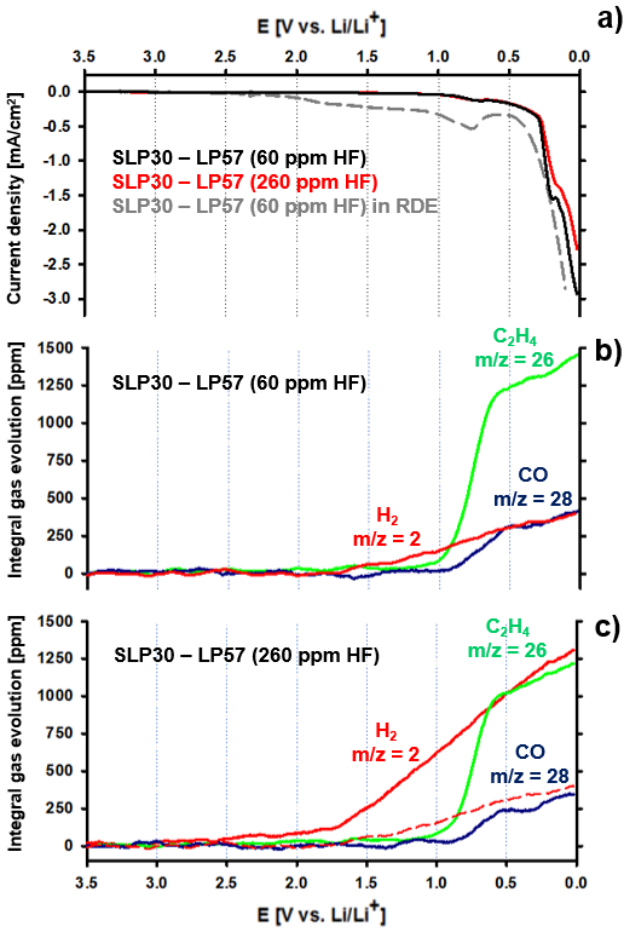

Figure 5: Electrocatalytic transformation of HF to LiF and H_2 on real graphite sample. a) Electrochemical response of SLP30 graphite in 1M $LiPF_6$ in a real graphite//LFP cell (black and red curves), measured at 0.2 mV/s and in the RDE configuration of our 3-electrode electrochemical cell (gray curve), measured at 50 mV/s. b-c) OEMS measurements of gas evolution from SLP30 graphite electrodes during the potential scan 3.5-0 V vs Li/Li^+ in 1M $LiPF_6$ (b) with 60 ppm HF and (c) with 260 ppm HF. The dashed red line in (c) is the H_2 trace from (b), shown for comparison.

References

1. Ross, P. N. & Lipkowski, J. *Structure of Electrified Interfaces*. (VCH Publishers, Inc., 1993).

2. Stamenkovic, V. R., Strmcnik, D., Lopes, P. P. & Markovic, N. M. Energy and fuels from electrochemical interfaces. *Nat Mater* **16,** 57–69 (2017).

3. Wieckowski, A. *Interfacial Electrochemistry*. (Marcel Dekker, Inc., 1999).

4. Marković, N. & Ross, P. N. Surface science studies of model fuel cell electrocatalysts. *Surf. Sci. Rep.* **45,** 117–229 (2002).

5. Nørskov, J. K., Bligaard, T., Rossmeisl, J. & Christensen, C. H. Towards the computational design of solid catalysts. *Nat. Chem.* **1,** 37–46 (2009).

6. An, S. J. *et al.* The state of understanding of the lithium-ion-battery graphite solid electrolyte interphase (SEI) and its relationship to formation cycling. *Carbon N. Y.* **105,** 52–76 (2016).

7. Peled, E. & Menkin, S. Review—SEI: Past, Present and Future. *J. Electrochem. Soc.* **164,** A1703–A1719 (2017).

8. Verma, P., Maire, P. & Novák, P. A review of the features and analyses of the solid electrolyte interphase in Li-ion batteries. *Electrochim. Acta* **55,** 6332–6341 (2010).

9. Nie, M., Abraham, D. P., Chen, Y., Bose, A. & Lucht, B. L. Silicon solid electrolyte interphase (SEI) of lithium ion battery characterized by microscopy and spectroscopy. *J. Phys. Chem. C* **117,** 13403–13412 (2013).

10. Owejan, J. E., Owejan, J. P., Decaluwe, S. C. & Dura, J. A. Solid electrolyte interphase in Li-ion batteries: Evolving structures measured in situ by neutron reflectometry. *Chem. Mater.* **24,** 2133–2140 (2012).

11. Soto, F. A., Ma, Y., Martinez De La Hoz, J. M., Seminario, J. M. & Balbuena, P. B. Formation and Growth Mechanisms of Solid-Electrolyte Interphase Layers in Rechargeable Batteries. *Chem. Mater.* **27,** 7990–8000 (2015).

12. Xu, K. Nonaqueous Liquid Electrolytes for Lithium-Based Rechargeable Batteries Nonaqueous Liquid Electrolytes for Lithium-Based Rechargeable Batteries. *Chem. Rev.* **104,** 4303–4417 (2004).

13. Aurbach, D. Review of selected electrode – solution interactions which determine the performance of Li and Li ion batteries. *J. Power Sources* **89,** 206–218 (2000).

14. Edström, K., Herstedt, M. & Abraham, D. P. A new look at the solid electrolyte interphase on graphite anodes in Li-ion batteries. *J. Power Sources* **153,** 380–384 (2006).

15. Zhang, B. *et al.* Role of 1,3-propane sultone and vinylene carbonate in solid electrolyte interface formation and gas generation. *J. Phys. Chem. C* **119,** 11337–11348 (2015).

16. Leroy, S., Martinez, H., Dedryvère, R., Lemordant, D. & Gonbeau, D. Influence of the lithium salt

nature over the surface film formation on a graphite electrode in Li-ion batteries: An XPS study. *Appl. Surf. Sci.* **253,** 4895–4905 (2007).

17. Leroy, S. *et al.* Surface film formation on a graphite electrode in Li-ion batteries: AFM and XPS study. *Surf. Interface Anal.* **37,** 773–781 (2005).

18. Aurbach, D., Zinigrad, E., Cohen, Y. & Teller, H. A short review of failure mechanisms of lithium metal and lithiaded graphite anodes in liquid electrolyte solutions. *Solid State Ionics* **148,** 405–416 (2002).

19. Aurbach, D., Markovsky, B., Shechter, A., Ein-Eli, Y. & Cohen, H. A Comparative Study of Synthetic Graphite and Li Electrodes in Electrolyte Solutions Based on Ethylene Carbonate-Dimethyl Carbonate Mixtures. *J. Electrochem. Soc.* **143,** 3809–3820 (1996).

20. Lee, H., Cho, J.-J., Kim, J. & Kim, H.-J. Comparison of Voltammetric Responses over the Cathodic Region in LiPF[sub 6] and LiBETI with and without HF. *J. Electrochem. Soc.* **152,** A1193 (2005).

21. Terborg, L. *et al.* Investigation of thermal aging and hydrolysis mechanisms in commercial lithium ion battery electrolyte. *J. Power Sources* **242,** 832–837 (2013).

22. Kawamura, T., Okada, S. & Yamaki, J. ichi. Decomposition reaction of LiPF6-based electrolytes for lithium ion cells. *J. Power Sources* **156,** 547–554 (2006).

23. Aurbach, D. *et al.* Recent studies on the correlation between surface chemistry, morphology, three-dimensional structures and performance of Li and Li-C intercalation anodes in several important electrolyte systems. *J. Power Sources* **68,** 91 (1997).

24. Plakhotnyk, A. V., Ernst, L. & Schmutzler, R. Hydrolysis in the system LiPF 6 - Propylene carbonate - Dimethyl carbonate - H 2O. *J. Fluor. Chem.* **126,** 27–31 (2005).

25. Tsuyoshi, Nakajima; Henri, G. *Fluorinated Materials for Energy Conversion*. (Elsevier B.V., 2005).

26. Lux, S. F. *et al.* The mechanism of HF formation in LiPF6 based organic carbonate electrolytes. *Electrochem. commun.* **14,** 47–50 (2012).

27. Aurbach, D. Electrode-solution interactions in Li-ion batteries: A short summary and new insights. *J. Power Sources* **119–121,** 497–503 (2003).

28. Zhang, Z. & Zhang, S. S. *Rechargeable Batteries: Materials, Technologies and New Trends*. (Springer International Publishing, 2015).

29. Wang, R., Li, X., Wang, Z. & Guo, H. Manganese dissolution from LiMn2O4 cathodes at elevated temperature: methylene methanedisulfonate as electrolyte additive. *J. Solid State Electrochem.* **20,** 19–28 (2016).

30. Pieczonka, N. P. W. *et al.* Understanding Transition-Metal Dissolution Behavior in $LiNi_{0.5}Mn_{1.5}O_4$ High-Voltage Spinel for Lithium Ion Batteries. *J. Phys. Chem. C* **117,** 15947–15957 (2013).

31. Kang, S. J., Yu, S., Lee, C., Yang, D. & Lee, H. Effects of electrolyte-volume-to-electrode-area ratio on redox behaviors of graphite anodes for lithium-ion batteries. *Electrochim. Acta* **141,** 367–373 (2014).

32. Strmcnik, D. *et al.* When Small is Big: The Role of Impurities in Electrocatalysis. *Top. Catal.* **58,** 1174–1180 (2015).

33. Marković, N. ., Gasteiger, H. ., Grgur, B. . & Ross, P. . Oxygen reduction reaction on Pt(111): effects of bromide. *J. Electroanal. Chem.* **467,** 157–163 (1999).

34. Strmcnik, D. S. *et al.* Unique activity of platinum adislands in the CO electrooxidation reaction. *J. Am. Chem. Soc.* **130,** 15332–15339 (2008).

35. Subbaraman, R. *et al.* Origin of Anomalous Activities for Electrocatalysts in Alkaline Electrolytes. *J. Phys. Chem. C* **116,** 22231–22237 (2012).

36. Vetter, K. J. *Electrochemical kinetics : theoretical and experimental aspects*. (Academic Press, 1967).

37. Thiel, P. a, Madey, T. E. & Sloan, A. P. The interaction of water with solid surfaces: Fundamental aspects. *Surf. Sci. Rep.* **7,** 211–385 (1987).

38. Henderson, M. A. The interaction of water with solid surfaces: fundamental aspects revisited. *Surf. Sci. Rep.* **46,** 1–308 (2002).

39. Trasatti, S. Work function, electronegativity, and electrochemical behaviour of metals: III. Electrolytic hydrogen evolution in acid solutions. *Electroanal. Chem. Interfacial Electrochem.* **39,** 163–184 (1972).

40. Greeley, J., Jaramillo, T. F., Bonde, J., Chorkendorff, I. & Nørskov, J. K. Computational high-throughput screening of electrocatalytic materials for hydrogen evolution. *Nat. Mater.* **5,** 909–913 (2006).

41. Strmcnik, D., Lopes, P. P., Genorio, B., Stamenkovic, V. R. & Markovic, N. M. Design principles for hydrogen evolution reaction catalyst materials. *Nano Energy* **29,** 29–36 (2016).

42. Staszak-Jirkovský, J. *et al.* Water as a Promoter and Catalyst for Dioxygen Electrochemistry in Aqueous and Organic Media. *ACS Catal.* **5,** 6600–6607 (2015).

43. Maibach, J., Lindgren, F., Eriksson, H., Edström, K. & Hahlin, M. Electric Potential Gradient at the Buried Interface between Lithium-Ion Battery Electrodes and the SEI Observed Using Photoelectron Spectroscopy. *J. Phys. Chem. Lett.* **7,** 1775–1780 (2016).

44. Matsuoka, O. *et al.* Ultra-thin passivating film induced by vinylene carbonate on highly oriented pyrolytic graphite negative electrode in lithium-ion cell. *J. Power Sources* **108,** 128–138 (2002).

45. Alliata, D., Kötz, R., Novák, P. & Siegenthaler, H. Electrochemical SPM investigation of the solid electrolyte interphase film formed on HOPG electrodes. *Electrochem. commun.* **2,** 436–440 (2000).

46. Jeong, S.-K., Inaba, M., Abe, T. & Ogumi, Z. Surface Film Formation on Graphite Negative Electrode in Lithium-Ion Batteries: AFM Study in an Ethylene Carbonate-Based Solution. *J. Electrochem. Soc.* **148,** A989 (2001).

47. Domi, Y. *et al.* Electrochemical AFM Observation of the HOPG Edge Plane in Ethylene Carbonate-Based Electrolytes Containing Film-Forming Additives. *J. Electrochem. Soc.* **159,** A1292–A1297 (2012).

48. Domi, Y. *et al.* In situ AFM study of surface film formation on the edge plane of HOPG for lithium-ion batteries. *J. Phys. Chem. C* **115,** 25484–25489 (2011).

49. Peled, E. *et al.* Composition, depth profiles and lateral distribution of materials in the SEI built on HOPG-TOF SIMS and XPS studies. *J. Power Sources* **97–98,** 52–57 (2001).

50. Metzger, M., Strehle, B., Solchenbach, S. & Gasteiger, H. A. Origin of H_2 Evolution in LIBs: H_2O Reduction vs. Electrolyte Oxidation. *J. Electrochem. Soc.* **163,** A798–A809 (2016).

51. Mortensen, J. J., Hansen, L. B. & Jacobsen, K. W. Real-space grid implementation of the projector augmented wave method. *Phys. Rev. B - Condens. Matter Mater. Phys.* **71,** 1–11 (2005).

52. Enkovaara, J. *et al.* Electronic structure calculations with GPAW: a real-space implementation of the projector augmented-wave method. *J. Phys. Condens. Matter* **22,** 253202 (2010).

53. Hjorth Larsen, A. *et al.* The atomic simulation environment—a Python library for working with atoms. *J. Phys. Condens. Matter* **29,** 273002 (2017).

54. Hammer, B., Hansen, L. & Nørskov, J. Improved adsorption energetics within density-functional theory using revised Perdew-Burke-Ernzerhof functionals. *Phys. Rev. B* **59,** 7413–7421 (1999).

55. Hansen, M. H. & Rossmeisl, J. pH in Grand Canonical Statistics of an Electrochemical Interface. *J. Phys. Chem. C* **120,** 29135–29143 (2016).

Acknowledgements

This research was sponsored by BMW Technology Corporation under contract number. The research was conducted at Argonne National Laboratory, a US Department of Energy Office of Science laboratory, operated by UChicago Argonne, LLC, under contract no. DE-AC02-06CH11357 and in part at the Technische Universität, München. We acknowledge support from the Office of Science, Office of Basic Energy Sciences and Materials Sciences and Engineering Division. We also thank Carol Thompson and Hoydoo You for their help with AFM and CTR measurements.

Author contributions

D.S., J.G.C., H.G. and N.M.M. conceived and designed the experiments, D.S., J.G.C., D.H. M.Z., P.M. P.P.L., and B.G. performed the experiments, I.E.C., T.O. and J.R. performed the calculations, D.S., J.G.C., I.E.C., F.M., B.K.A., J.R., H.G., V.R.R and N.M. discussed the results and wrote the paper.

Competing financial interests

The authors declare no competing financial interests.